ChemComm

COMMUNICATION

View Article Online
View Journal | View Issue

Cite this: *Chem. Commun.*, 2025, **61**, 17428

Received 10th September 2025,
Accepted 6th October 2025

DOI: 10.1039/d5cc05230k

rsc.li/chemcomm

Boosting the efficiency of Ruddlesden–Popper tin perovskite solar cells through ethylenediamine dihydroiodide-mediated phase modulation

Jorim Okoth Obila,[a] Chunging Li,[a] Masatoshi Yanagida,[b] Yasuhiro Shirai[b] and Yuko Takeoka*[a]

Quasi-two-dimensional Ruddlesden–Popper tin perovskite solar cells (q-2D SnPSCs) show low power conversion efficiency (PCE) due to the formation of randomly oriented multiple lower-dimensional perovskite phases. Ethylenediamine dihydroiodide tuned the crystal orientation and modulated the formation of lower *n* members in RP tin perovskite films, resulting in q-2D SnPSCs with a PCE of 8.29%.

Tin perovskite solar cells (SnPSCs) have recently gained extraordinary attention from photovoltaic device researchers because of the unique photophysical properties of tin perovskite (SnP) materials. Apart from their reduced toxicity, SnP materials show robust optoelectronic properties and stable perovskite structures like their lead perovskite counterpart.[1] Recently, He and co-researchers achieved a certified power conversion efficiency (PCE) of 16.65%, which is the highest PCE reported for a SnPSC;[2] however, this efficiency still lags behind that of lead perovskite solar cells, which stand at a certified value of ~27%.[3] The low efficiency of SnPSCs is attributed to the ease of oxidation of Sn^{2+} ions in the perovskite absorber layer. The oxidation of Sn^{2+} ions leads to high p-doping and Sn vacancies, which are detrimental to the charge transfer in SnPSCs.[4] Also, the crystallization of the SnP film is fast and difficult to control because of the high Lewis acidity of Sn^{2+}.[1] Thus, depositing high-quality and stable SnP films for the fabrication of high-PCE and durable devices is complex.

The stability and performance of SnPSCs have been greatly improved in recent years with the introduction of bulky ammonium spacers to fabricate pure two-dimensional (2D) and quasi-two-dimensional (q-2D) Sn Ruddlesden–Popper (RP) perovskites with the formula $A_2A'_{n-1}Sn_nX_{3n+1}$, where A is a bulky ammonium cation such as butylammonium or phenethylammonium, A′ is a small monovalent cation such as formamidinium (FA) or methylammonium (MA), and X is a halide anion of Cl, Br, or I or a mixture of these halide anions.[5–8] The bulky ammonium cations are intrinsically hydrophobic and also capable of restricting ion migration in SnPSCs,[9] thus increasing the stability of SnPSCs.[10] However, the organic bulky ammonium cations are insulating and can restrict vertical charge movement in PSCs if not properly oriented, thereby lowering the PCE.[11] Thus, there is a need to exploit the spacer cations that induce stability and to identify methods of improving charge transport in q-2D and pure 2D PSCs to realize high-performing and stable SnPSCs.

The highest reported PCE for an RP q-2D SnPSC still stands at 10.36%,[12] which is inferior to the 16.65% reported for 2D/3D SnPSCs.[2] The reduced PCE is primarily due to poor crystal orientation, the formation of numerous lower-dimensional phases, and poor morphology due to the complex crystallization process in q-2D SnPs.[13] Most perovskite films are solution-processed, and solution-processed RP films exhibit multiple quantum wells (MQWs) due to phase segregation.[14] MQWs are common for RP phases with high *n* numbers. The MQWs result in impurity phases and substantial structural defects, which act as charge recombination centers, leading to devices with low stability and low PCEs.[15] The ability to fabricate q-2D SnPSCs with reduced quantum confinement (which can be achieved with high *n* numbers) and phase-pure QWs is critical if both high performance and stability are to be realized in RP SnPSCs.

In this work, we attempt to reduce the quantum confinement in q-2D SnPSCs by introducing a perovskite absorber layer with the formula $A_2A'_6Sn_7X_{22}$ into the SnPSC architecture. The SnP absorber material with such a high *n* value ($n = 7$) has not previously been explored by researchers, likely because the MQWs intensify with increasing *n* value. Soe *et al.* showed that the formation of $n = 7$ lead (Pb) perovskite crystals is marred by the formation of multiple *n* phases of $n = 2$, $n = 3$ and $n = \infty$;[16]

[a] *Faculty of Science and Engineering, Sophia University, 7-1 Kioi-cho, Chiyoda-ku, Tokyo, Japan. E-mail: y-tabuch@sophia.ac.jp*
[b] *Photovoltaic Materials Group, Centre for GREEN Research on Energy and Environmental Materials, National Institute for Materials Science (NIMS), 1-1 Namiki, Tsukuba, Ibaraki, Japan*

this can lead to MQWs. The numerous MQWs in high-n-value SnP can lead to unbalanced and mixed band alignment, which in turn can lead to charge transport barriers within the perovskite layer and result in diminished PCE.

Ethylenediamine dihydroiodide ($EDAI_2$) has previously been used as a surface passivator in SnPSCs.[17] $EDAI_2$ can control the rate of crystallization of 3D SnP films and thus improve perovskite absorber material quality.[18] For the first time, we fabricated q-2D SnPSCs with the general formula $A_2A'_6Sn_7X_{22}$, $PEA_2FA_6Sn_7I_{15.4}Br_{6.6}$, and used $EDAI_2$ to control its crystal orientation and formation of lower n members. The devices based on $PEA_2FA_6Sn_7I_{15.4}Br_{6.6}$ (n = 7) with the $EDAI_2$ additive achieved an efficiency as high as 8.29%, which is currently in the range of that of the best-performing q-2D SnPSCs.

X-ray diffraction (XRD) patterns for the q-2D SnP films with the chemical formula $PEA_2FA_6Sn_7I_{15.4}Br_{6.6}$, with and without $EDAI_2$ at various concentrations, were investigated to elucidate the effect of $EDAI_2$ on the crystal structure of q-2D SnP. The XRD patterns for all four prepared films showed diffraction peaks at 14.02° and 28.30° (Fig. 1(a)), corresponding to the (111) and (202) planes of a 2D RP.[18] The XRD patterns of the films also exhibited peaks at 3.9° and 5.3°, which are attributed to the n = 2 and n = 3 phases of the RP perovskite, respectively.[19] After $EDAI_2$ was added to the perovskite film, the peak at 3.9° shifted toward a lower angle (SI, Fig. S1), showing that EDA^{2+} was incorporated into the perovskite lattice.[18] Using the perovskite precursor solution with a concentration of 2 mg mL^{-1} $EDAI_2$ resulted in films with a diminished n = 3 phase, indicating that $EDAI_2$ could modulate the formation of multiple phases in the RP SnP films. The changes observed in the n = 2 and n = 3 phases could be because $EDAI_2$ forms strong hydrogen bonding with the perovskite components and also leads to the formation of "hollow" perovskite crystals with stabilized and well-oriented crystal structures.[20] The addition of $EDAI_2$ improved the film crystallinity as evident from the enhanced XRD-peak intensity. The full-width at half-maximum (FWHM) was reduced as shown in Fig. 1(b), further confirming improved crystallinity. The observed increase in crystallinity is critical for the deposition of high-quality and stable q-2D RP films for use in high-PCE photovoltaic devices.[21,22]

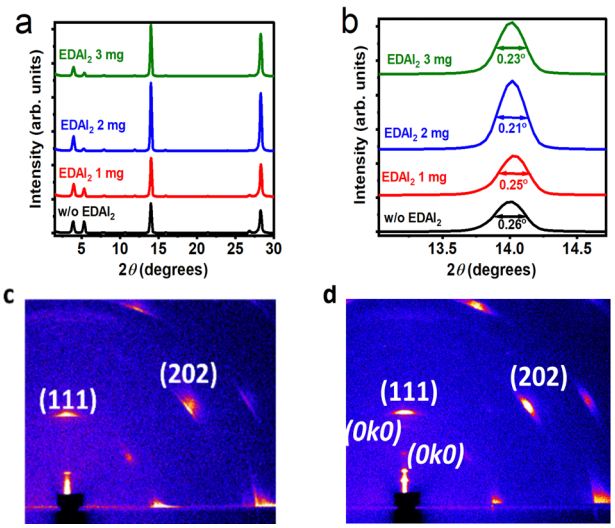

Fig. 1 (a) XRD patterns for $PEA_2FA_6Sn_7I_{15.4}Br_{6.6}$ films with different amounts of $EDAI_2$ and (b) an extraction of the peak around 14.0° for calculation of the full-width at half-maximum. GIWAXS images of (c) the control film and (d) a film with 1 mg mL^{-1} $EDAI_2$, acquired at an incidence angle of 0.5°.

Grazing-incidence wide-angle X-ray scattering (GIWAXS) measurement was used to confirm the crystal plane orientation of the films. GIWAXS images of the control film, and films containing 1 mg mL^{-1} $EDAI_2$ are shown in Fig. 1(c) and (d), respectively. The GIWAXS patterns of the films containing 2 and 3 mg mL^{-1} $EDAI_2$ are provided in the SI, Fig. S2(a) and (b), respectively. The control film did not show any orientation of the lower n members of the perovskite film despite the XRD pattern showing their existence, suggesting that the lower n members are randomly oriented. The GIWAXS patterns of the 1 mg mL^{-1} $EDAI_2$-based films showed improved crystal orientation, as indicated by their brighter Bragg spots (Fig. 1(d)). The GIWAXS patterns of the $EDAI_2$-based films also clearly show parallelly orientated lower-n phases, as indicated by the (0k0) reflections in Fig. 1(d) and Fig. S1(a), (b). The observed crystal orientation induced by $EDAI_2$ is attributable to the strong interaction between EDA^{2+} and Sn^{2+} to retard the rate of perovskite crystallization, leading to preferred crystal orientation.[23] EDA^{2+} and SnI_2 interaction was confirmed using X-ray photoelectron spectroscopy (XPS) (Fig. S3); the interaction was predicted from the shift of the Sn $3d_{3/2}$ peak to a lower binding energy upon the addition of $EDAI_2$ to the perovskite film.

The Scherrer formula, $D_{size} = K\lambda/(\beta \cos\theta)$, where D_{size} is the crystallite size or grain diameter, K is the Scherrer constant (K = 0.94), λ is the X-ray wavelength, β is the FWHM, and θ is the angle of diffraction, was used to determine the crystallite sizes in the deposited perovskite films. From the calculations, the crystallite sizes were found to be 34.26 nm, 35.05 nm, 40.62 nm, and 35.88 nm for the reference film and the samples with 1 mg mL^{-1}, 2 mg mL^{-1} and 3 mg mL^{-1} $EDAI_2$, respectively. The large crystallite size of the samples containing $EDAI_2$ indicates that these films have larger grain sizes.[24]

The Williamson–Hall formula, $\beta \cos\theta = 4\varepsilon \sin\theta + K\lambda/D_{size}$, where ε is the microstrain, was used to determine the microstrain in the films.[25] The Williamson–Hall formula was simplified to ε = (FWHM)/4 tan θ before it was used to determine the bulk microstrain values. The microstrain values were 8.6×10^{-3}, 8.4×10^{-3}, 7.2×10^{-3}, and 8.2×10^{-3} for the control film and the films with 1 mg mL^{-1}, 2 mg mL^{-1} and 3 mg mL^{-1} $EDAI_2$, respectively, using peaks located at ~14°. The films containing $EDAI_2$ showed a reduced lattice strain, which can help improve film stability and quality.[26]

The surface morphology of the films was investigated *via* scanning electron microscopy (SEM) (Fig. 2). The film without $EDAI_2$ (Fig. 2(a)) exhibited numerous pinholes, which is unfavorable to the PCE and stability of the SnPSCs.[19] The number of pinholes was substantially reduced when 1 mg mL^{-1} $EDAI_2$ was added to the film (Fig. 2(b)), indicating that $EDAI_2$ could passivate the q-2D SnP films. $EDAI_2$ induces uniform

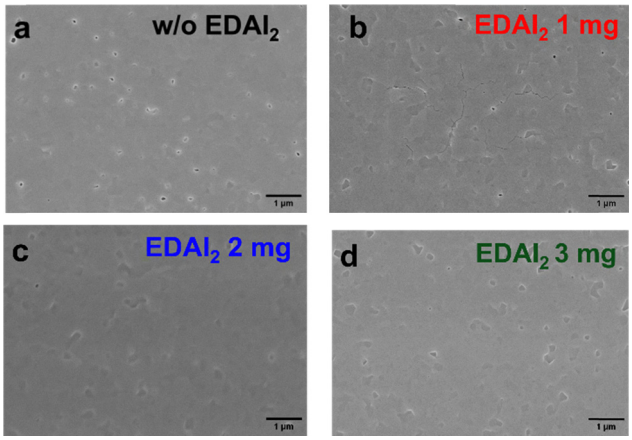

Fig. 2 SEM images of (a) a control film and films containing (b) 1 mg mL^{-1}, (c) 2 mg mL^{-1}, and (d) 3 mg mL^{-1} of $EDAI_2$.

nucleation and slows down crystal growth due to the interaction of its amino groups and the perovskite components, hence passivating the perovskite film surface.[1,20] At 2 mg mL^{-1} (Fig. 2(c)), $EDAI_2$ fully passivated the pinholes and resulted in a dense film, which, upon closer inspection, appeared like a double-layered film. The double layer may not necessarily be appropriate for devices because it can be a sign of a thicker insulating layer at the surface of the perovskite. The film showed intensified "potholes" when excess (3 mg mL^{-1}) $EDAI_2$ was used (Fig. 2(d)).

UV-Vis absorption measurements were conducted to determine the effect of $EDAI_2$ on the optical properties of the q-2D RP SnP films (Fig. 3). The absorption onset of the control film was ~800 nm (band gap of 1.55 eV) and that of the film containing $EDAI_2$ was ~826 nm (band gap of 1.50 eV) (Fig. 3(a) and SI Fig. S4), showing a slight reduction in film bandgap due to a reduction in the quantum confinement because of the elimination or modulation of wide-bandgap multiple lower-dimensional phases in the perovskite film.[27]

Photoluminescence (PL) measurements were conducted from the front side of the films (the perovskite facing the Xe lamp direction) (Fig. 3(b)). The PL spectrum of the control film shows a broad diminished peak; in addition, the peak exhibits a shoulder on the lower-wavelength side, which is speculatively

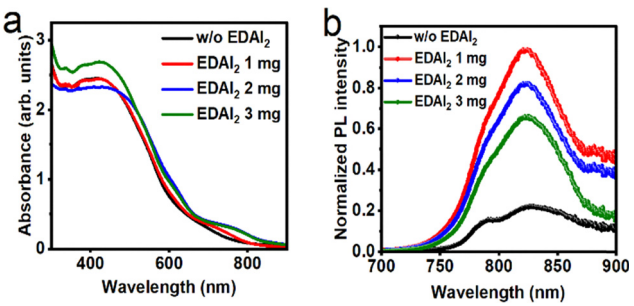

Fig. 3 (a) The UV-Vis absorption spectra of quasi-2D SnP films. (b) The photoluminescence spectra of the deposited SnP films, acquired at an excitation wavelength of 525 nm.

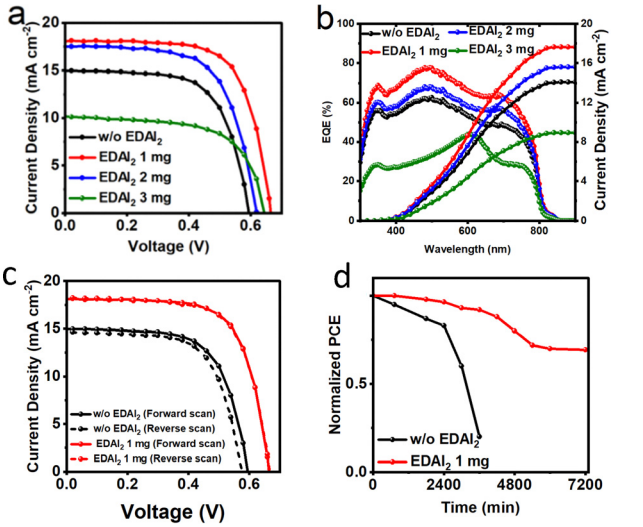

Fig. 4 (a) Forward-scan current density–voltage (*J*–*V*) curves of the devices without and with various amounts of $EDAI_2$. (b) EQE curves. (c) *J*–*V* curves of the control and 1 mg mL^{-1} $EDAI_2$-based solar cells measured in the forward and reverse scan directions. (d) Normalized PCE stability of the devices measured outside an inert environment.

attributed to lower *n*-phases.[28] The PL intensity of samples containing $EDAI_2$ increased substantially, and the shoulder disappeared, which can be attributed to the elimination of charge trap sites created by the existence of randomly oriented MQWs and pinholes in the perovskite layer.[29] The PL intensity reduced when excess $EDAI_2$ was added to the perovskite; this observation could be associated with the disruption of the lattice structure of the perovskite induced by excess $EDAI_2$. According to the GIWAXS data, the 1 mg mL^{-1} $EDAI_2$ showed brighter and smaller Bragg spots, signifying enhanced crystallinity, better crystal orientation and reduced defect density when compared to the other films containing excess $EDAI_2$.

The p–i–n structured q-2D SnPSCs with a $PEA_2FA_6Sn_7I_{15.4}Br_{6.6}$ absorber layer were fabricated, and their photovoltaic performances were determined to elucidate the effect of $EDAI_2$ on the PCE parameters of the q-2D SnPSCs (Fig. 4a). The champion control device demonstrated a PCE of 5.83% with a fill factor (FF) of 65.36%, an open-circuit voltage (V_{OC}) of 0.59 V, and a short-circuit current density (J_{SC}) of 14.99 mA cm^{-2}. The 1 mg mL^{-1} $EDAI_2$ showed the best performance, with a PCE as high as 8.29%, an FF of 69.03%, a V_{OC} of 0.67 V, and a J_{SC} of 18.05 mA cm^{-2}. The improved V_{OC} and FF of the 1 mg mL^{-1} $EDAI_2$ can be associated with reduced non-radiative recombination in the solar cells, as shown in the PL data.[30] In contrast, the 2 and 3 mg mL^{-1} $EDAI_2$-based devices showed reduced PCEs, 7.02% (a V_{OC} of 0.62, an FF of 64.61%, and a J_{SC} of 17.52 mA cm^{-2}) and 4.17% (a V_{OC} of 0.64, an FF of 63.61%, and a J_{SC} of 10.18 mA cm^{-2}), respectively, because excess $EDAI_2$ reduces the micro-crystallinity of q-2D SnP, which in turn increases nonradiative recombination centers in the q-2D SnP films as shown in the GIWAXS and PL data, respectively.

The J_{SC} values of the solar cells were confirmed using external quantum efficiency (EQE) measurement (Fig. 4b).

The integrated J_{SC} values of the control and 1 mg mL^{-1} $EDAI_2$-based solar cells were 14.57 mA cm^{-2} and 17.66 mA cm^{-2}, respectively, comparable to the J_{SC} values from the J–V curve measurements. The statistical data of the control and 1 mg mL^{-1} $EDAI_2$-based solar cells are presented in SI Fig. S5 and Table S1 to confirm the reproducibility.

Hysteresis observed in PSCs usually originates from defects within the solar cells. In the case of 2D SnPSCs, the dominant defects are related to random orientation of the spacer layers, which lead to MQWs. We investigated the hysteresis in the best-performing control and $EDAI_2$-based SnPSCs by measuring the photovoltaic performance of the devices in both the forward and reverse directions (Fig. 4c and SI Table S2). Hysteresis levels were estimated using the hysteresis index (HI) formula.[31] The best-performing $EDAI_2$-based solar cell showed a reduced hysteresis index of 1.09%, whereas the reference solar cell showed a magnified hysteresis index of 5.32%; the reduced hysteresis levels of the $EDAI_2$-based devices are a result of improved SnP film crystal orientation induced by $EDAI_2$. Stability tests were conducted for unencapsulated devices (Fig. 4d); the devices were stored outside an inert environment during the measurements. The humidity range during the tests was 30–40%, and the temperature range was 21–24 °C. The devices based on 1 mg mL^{-1} $EDAI_2$ showed better stability, retaining 70% of their original efficiency after 7200 min. The reduced stability of the reference device is due to magnified nonradiative charge recombination because of random crystal orientation in the perovskite layer.

The addition of $EDAI_2$ to the perovskite precursor solution helped in controlling the film crystallization process, resulting in improved crystallinity, morphology, and optical properties. $EDAI_2$ addition also helped in tuning the orientation of lower-dimensional multiple phases resulting from 2D RP SnP with high n values such as 7. The phase tuning was due to the interaction between PEA^+, EDA^+ and SnI_2. As a result, the $EDAI_2$-based devices achieved an efficiency of 8.29% and an efficiency retention as high as 70% for 7200 min outside an inert environment.

This work was supported in part by the Japan Science and Technology Agency (JST)-ALCA-Next Program (Grant No. JPMJAN23B2).

Conflicts of interest

There are no conflicts to declare.

Data availability

Data supporting this article have been included in the supplementary information (SI). Supplementary information is available. See DOI: https://doi.org/10.1039/d5cc05230k.

Notes and references

1 W. Gao, R. Huang, H. Dong, W. Li, Z. Wu, Y. Chen and C. Ran, *Chem. Soc. Rev.*, 2025, **54**, 1384–1428.
2 D. He, P. Chen, J. A. Steele, Z. Wang, H. Xu, M. Zhang, S. Ding, C. Zhang, T. Lin, F. Kremer, H. Xu, M. Hao and L. Wang, *Nat. Nanotechnol.*, 2025, **20**, 779–786.
3 NREL, Best Research-Cell Efficiency chart, https://www.nrel.gov/pv/cell-efficiency.html. (Accessed August 2025).
4 J. Zhang and Y. Zhong, *Angew. Chem., Int. Ed.*, 2022, **61**, e202212002.
5 Y. Shi, Z. Zhu, D. Miao, Y. Ding and Q. Mi, *ACS Energy Lett.*, 2024, **9**, 1895–1897.
6 B. Bin Yu, Z. Chen, Y. Zhu, Y. Wang, B. Han, G. Chen, X. Zhang, Z. Du and Z. He, *Adv. Mater.*, 2021, **33**, 2102055.
7 M. Yin, H. Yao, C. Wu, P. Yan, L. Ding and F. Hao, *Chem. Eng. J.*, 2025, **511**, 162111.
8 M. A. K. Sheikh, D. Kowal, M. H. Mahyuddin, R. Cala', E. Auffray, M. E. Witkowski, M. Makowski, W. Drozdowski, H. Wang, C. Dujardin, D. Cortecchia and M. D. Birowosuto, *J. Phys. Chem. C*, 2023, **127**, 10737–10747.
9 D. Hishida, T. H. Chowdhury, R. Shimono, A. Saeki, G. Uzurano, A. Fujii, M. Yoshizawa-Fujita, M. Rikukawa and Y. Takeoka, *ACS Appl. Energy Mater.*, 2025, **8**, 5738–5744.
10 T. Zhou, H. Lai, T. Liu, D. Lu, X. Wan, X. Zhang, Y. Liu and Y. Chen, *Adv. Mater.*, 2019, **31**, 1901242.
11 F. Yang, R. Zhu, Z. Zhang, Z. Su, W. Zuo, B. He, M. H. Aldamasy, Y. Jia, G. Li, X. Gao, Z. Li, M. Saliba, A. Abate and M. Li, *Adv. Mater.*, 2024, **36**, 2308655.
12 J. Qiu, Y. Lin, X. Ran, Q. Wei, X. Gao, Y. Xia, P. Müller-Buschbaum and Y. Chen, *Sci. China: Chem.*, 2021, **64**, 1577–1585.
13 D. H. Cao, C. C. Stoumpos, T. Yokoyama, J. L. Logsdon, T. Bin Song, O. K. Farha, M. R. Wasielewski, J. T. Hupp and M. G. Kanatzidis, *ACS Energy Lett.*, 2017, **2**, 982–990.
14 L. Mao, R. M. Kennard, B. Traore, W. Ke, C. Katan, J. Even, M. L. Chabinyc, C. C. Stoumpos and M. G. Kanatzidis, *Chemistry*, 2019, **5**, 2593–2604.
15 Y. Guo, H. Yao, M. Zhang and F. Hao, *Sol. RLL*, 2024, **8**(10), 2400121.
16 C. M. Myae Soe, G. P. Nagabhushana, R. Shivaramaiah, H. Tsai, W. Nie, J. C. Blancon, F. Melkonyan, D. H. Cao, B. Traoré, L. Pedesseau, M. Kepenekian, C. Katan, J. Even, T. J. Marks, A. Navrotsky, A. D. Mohite, C. C. Stoumpos and M. G. Kanatzidis, *Proc. Natl. Acad. Sci. U. S. A.*, 2019, **116**, 58–66.
17 S. Sandhu, R. Singh, K. Yoo, M. Kumar and J. J. Lee, *J. Power Sources*, 2021, **491**, 229574.
18 Y. Jiang, Z. Lu, S. Zou, H. Lai, Z. Zhang, J. Luo, Y. Huang, R. He, J. Jin, Z. Yi, Y. Luo, W. Wang, C. Wang, X. Hao, C. Chen, X. Wang, Y. Wang, S. Ren, T. Shi, F. Fu and D. Zhao, *Nano Energy*, 2022, **103**, 107818.
19 Z. Kang, K. Wang, L. Zhang, Y. Yang, J. Wu, Y. Tong, P. Yan, Y. Chen, H. Qi, K. Sun, P. Müller-Buschbaum, X. Zhang, J. Shang and H. Wang, *Small*, 2024, **20**(43), 2402028.
20 G. A. Tosado, E. Zheng and Q. Yu, *Mater. Adv.*, 2020, **1**, 3507–3517.
21 Z. Kang, P. Feng, K. Wang, L. Zhang, R. Meng, Y. Chen, J. Wu, F. Yang, X. Zhang, T. Li, J. Shang, Y. Tong and H. Wang, *Energy Environ. Sci.*, 2025, **18**, 4108–4119.
22 C. Li, T. H. Chowdhury, M. Yoshizawa-Fujita, M. Rikukawa, M. Yanagida, Y. Shirai and Y. Takeoka, *Chem. Commun.*, 2025, **61**, 6462–6465.
23 Y. Huang, Y. Jiang, S. Zou, Z. Zhang, J. Jin, R. He, W. Hu, S. Ren and D. Zhao, *ACS Appl. Mater. Interfaces*, 2023, **15**, 15775–15784.
24 J. Liu, S. Wang, W. Zhu, Z. Tang, L. Ding and F. Hao, *Chem. Eng. J.*, 2023, **453**, 139975.
25 G. C. Halford, Q. Deng, A. Gomez, T. Green, J. M. Mankoff and R. A. Belisle, *ACS Appl. Mater. Interfaces*, 2022, **14**, 4335–4343.
26 D. K. Lee, K. Fykouras, T. Kodalle, R. F. Moral, C. P. Schwartz, N. Tamura, K. V. Lawler, L. Leppert and C. M. Sutter-Fella, *ACS Energy Lett.*, 2025, **10**, 1039–1049.
27 A. Ummadisingu, S. Meloni, A. Mattoni, W. Tress and M. Grätzel, *Angew. Chem., Int. Ed.*, 2021, **60**, 21368–21376.
28 A. A. Sutanto, N. Drigo, V. I. E. Queloz, I. Garcia-Benito, A. R. Kirmani, L. J. Richter, P. A. Schouwink, K. T. Cho, S. Paek, M. K. Nazeeruddin and G. Grancini, *J. Mater. Chem. A*, 2020, **8**, 2343–2348.
29 A. Semerci, A. Buyruk, S. Emin, R. Hooijer, D. Kovacheva, P. Mayer, M. A. Reus, D. Blätte, M. Günther, N. F. Hartmann, S. Lotfi, J. P. Hofmann, P. Müller-Buschbaum and T. Bein, and T, *Adv. Opt. Mater.*, 2023, **11**, 2300267.
30 S. W. Cho, P. Pandey, B. Huān, J. Liu, H. G. Lim, H. Ahn, S. Yoon, J. Ryu, Q. Shen, S. Hayase and D. W. Kang, *InfoMat*, 2025, e70052.
31 M. Minbashi and E. Yazdani, *Sci. Rep.*, 2022, **12**, 14916.